ISSN 0965-5425, Computational Mathematics and Mathematical Physics, 2016, Vol. 56, No. 9, pp. 1620–1630. © Pleiades Publishing, Ltd., 2016.
Original Russian Text © I.E. Kvasov, V.B. Leviant, I.B. Petrov, 2016, published in Zhurnal Vychislitel'noi Matematiki i Matematicheskoi Fiziki, 2016, Vol. 56, No. 9, pp. 1645–1656.

Numerical Study of Wave Propagation in Porous Media with the Use of the Grid-Characteristic Method

I. E. Kvasov*, V. B. Leviant, and I. B. Petrov

Moscow Institute of Physics and Technology (State University), Institutskii per. 9, Dolgoprudnyi, Moscow oblast, 141700 Russia

**e-mail: i.kvasov@gmail.com*

Received July 8, 2015; in final form, February 8, 2016

Abstract—Elastic wave propagation in a porous medium is numerically studied by applying the grid-characteristic method. On the basis of direct measurements of reflected and transmitted wave amplitudes, the reflection and decay coefficients are investigated as depending on the degree of porosity (percentage of the pore volume) and on the type of the filling substance (solid, liquid, or nothing). The reflection and decay coefficients are shown to be closely related to the porosity of the medium, which can be used in geological applications (estimation of porosity) and engineering applications (acoustic response attenuation).

Keywords: continuum mechanics, numerical methods, porous media, grid-characteristic method.

DOI: 10.1134/S0965542516090116

The porosity of a medium is defined as the ratio of the volume of all pores to the entire volume of the medium. This characteristis is used in seismic exploration to analyze seismis responces of porous rock and in engineering applications to study soundproof covers. For various types of porous media, the effects of factors, such as viscosity, fluid flow, and saturation, on the velocity and attenuation of elastic waves were examined in Gurevich and his colleagues' works [1]. Elastic wave propagation in porous media is usually simulated using shock-capturing finite-difference methods. The grid-characteristic methods [2, 3] used in this paper make it possible to consider all inhomogeneous inclusions, including pores, to obtain an adequate wave pattern. The goals of this work are as follows:

(1) To quantitatively estimate the relation between the porosity of the medium and response characteristics, such as the reflection and decay coefficients, by rigorously solving continuum mechanics equations (with boundary conditions specified on the pore–medium interfaces).

(2) To estimate the influence exerted by various pore fillers (solid, liquid, or no filler) on the reflection and decay coefficients.

1. SYSTEM OF GOVERNING EQUATIONS

To study elastic wave propagation caused by an incident (compressional) wavefront transmitted through a porous medium, we used a hybrid grid-characteristic method on nonuniform triangular meshes. The medoum was assumed to be ideal, isotropic, linear, and elastic. These assumptions correspond to the local equation of motion

$$\rho\dot{\mathbf{v}} = \nabla \cdot \mathbf{T},$$

where ρ is the material density, $\mathbf{v}$ is the velocity of the medium at a given point, ∇ is the gradient with respect to spatial coordinates, and $\mathbf{T}$ is the Cauchy stress tensor.

We introduce the symmetric small strain tensor

$$\mathbf{e} = \frac{1}{2}(\nabla \otimes \mathbf{u} + \mathbf{u} \otimes \nabla),$$

where $\mathbf{u}$ is the displacement field ($\mathbf{x} = \mathbf{X} + \mathbf{u}$, where $\mathbf{x}$ is the position of some point of the body at the current time and $\mathbf{X}$ is its position at the initial time) and $\otimes$ is the tensor product operator: $(\mathbf{a} \otimes \mathbf{b})_{ij} = a_i b_j$. In the product $(\mathbf{u} \otimes \nabla)$, the fileld $\mathbf{u}$, rather than the subsequent multipliers, is subject to differentiation:

$$(\nabla \otimes \mathbf{u} + \mathbf{u} \otimes \nabla)_{ij} = \nabla_i u_j + \nabla_j u_i.$$

The linear elasticity of the material implies the stress–strain relationship

$$\mathbf{T} = \lambda(\mathbf{e} : \mathbf{I}) + 2\mu\mathbf{e},$$

where λ and μ are the Lamé constants, which determine the properties of the elastic material (there are one-to-one formulas relating the Lamé constants to Young's modulus and Poisson's ratio), $\mathbf{I}$ is the unit tensor, and : denotes the double convolution:

$$\mathbf{a} : \mathbf{b} = \sum_{i,j} a_{ij} b_{ij}.$$

To obtain a closed system of differential equations for velocities and stresses, we need to differentiate the stress–strain relationship:

$$\rho\dot{\mathbf{v}} = \nabla \cdot \mathbf{T}, \quad \dot{\mathbf{T}} = \lambda(\nabla \cdot \mathbf{v})\mathbf{I} + \mu(\nabla \otimes \mathbf{v} + \mathbf{v} \otimes \nabla).$$

In the considered model, the material characteristics ρ, λ, and μ are assumed to be independent of the velocities or stresses.

2. NUMERICAL METHOD

The problem was solved numerically by applying the grid-characteristic method [2], which takes into account the indicated physical features of the problem (i.e., discontinuity propagation along characteristic surfaces) and provides a basis for numerical algorithms that do not fail on boundaries and on material interfaces.

The dimensional splitting method described in [2] was used to pass from the multidimensional system of partial differential equations to several one-dimensional systems of equations solved sequentially at every integration step.

2.1. Canonical Form of the Differential Equations

Before applying the grid-characteristic method, the dynamical system of solid mechanics equations is brought to canonical form:

$$\dot{\mathbf{u}} + \sum_j \mathbf{A}_j \frac{\partial \mathbf{u}}{\partial \xi_j} = 0,$$

where $\mathbf{u}$ is the vector of sought functions:

$$\mathbf{u} = \{\upsilon_1, \upsilon_2, \upsilon_3, \sigma_{11}, \sigma_{12}, \sigma_{13}, \sigma_{22}, \sigma_{23}, \sigma_{33}\}^{\mathrm{T}}.$$

The difference schemes involve the matrix $\mathbf{A}_j$ and various functions of $\mathbf{A}_j$. To avoid matrix inversion and the approximate computation of matrix eigenvalues and eigenvectors in the grid-characteristic difference schemes, $\mathbf{A}_j$ and its spectral decomposition are represented in the explicit form obtained in [4].

We will use some notation introduced in [4]. Let (ξ_1, ξ_2, ξ_3) be an arbitrary basis for some curvilinear coordinate system. Most frequently, the axis directions are chosen depending on the local configuration of grid nodes by using the coordinates of the nodes nearest to a given one. In this paper, in the case of triangular and tetrahedral grids, the coordinate system at every integration step is chosen at random in order to reduce the possible anisotropy of the method. In the case of hexahedral grids, the coordinate axes are chosen along the grid lines. Let

$$\mathbf{q}_j \equiv \frac{\partial \xi_j}{\partial \mathbf{x}},$$

where $(\mathbf{x}_1, \mathbf{x}_2, \mathbf{x}_3)$ is a fixed Cartesian coordinate system. Thus, $(\mathbf{q}_1, \mathbf{q}_2, \mathbf{q}_3)$ is a biorthogonal basis with respect to (ξ_1, ξ_2, ξ_3):

$$\mathbf{q}_1 = \frac{[\xi_2, \xi_3]}{(\xi_1, \xi_2, \xi_3)}, \quad \mathbf{q}_2 = \frac{[\xi_3, \xi_1]}{(\xi_1, \xi_2, \xi_3)}, \quad \mathbf{q}_3 = \frac{[\xi_1, \xi_2]}{(\xi_1, \xi_2, \xi_3)}.$$

Here, each numerator is a vector cross product and each denominator is a mixed vector product. Each of the vectors $\mathbf{q}_j$ is associated with an orthonormal basis $(\mathbf{n}_{j,0}, \mathbf{n}_{j,1}, \mathbf{n}_{j,2})$, where $\mathbf{n}_{j,0}$ is codirectional with $\mathbf{q}_j$:

$$\mathbf{n}_{j,0} = \frac{\mathbf{q}_j}{\|\mathbf{q}_j\|}, \quad l_j = \|\mathbf{q}_j\|,$$

while the unit vectors $\mathbf{n}_{j,1}$ and $\mathbf{n}_{j,2}$ are chosen so as to obtain an orthonormal basis. In what follows, we omit the first index j and the second index 0 from $\mathbf{n}_{j,0}$, if they can be recovered from the context. Additionally, the symmetric matrices $\mathbf{N}_{ij} = \mathbf{N}_{ji}$ are defined as

$$\mathbf{N}_{ij} = \frac{1}{2}(\mathbf{n}_i \otimes \mathbf{n}_j + \mathbf{n}_j \otimes \mathbf{n}_i), \quad (i, j = 0, 1, 2).$$

Finally, let $c_1 = \sqrt{\dfrac{\lambda + 2\mu}{\rho}}$ be the longitudinal speed of sound in the elastic material, $c_2 = \sqrt{\dfrac{\mu}{\rho}}$ be the transverse speed of sound, and $c_3 = \sqrt{\dfrac{\lambda^2}{\rho(\lambda + 2\mu)}}$.

Let us write out closed-form expressions for the matrix $\mathbf{A}$ and its spectral decomposition $\mathbf{A} = \boldsymbol{\Omega}^{-1}\boldsymbol{\Lambda}\boldsymbol{\Omega}$, where $\boldsymbol{\Lambda} = \operatorname{diag}\{\lambda_i\}$ is a diagonal matrix composed of the eigenvalues of $\mathbf{A}$ and $\boldsymbol{\Omega}$ is the matrix composed of the corresponding eigenvectors of $\mathbf{A}$:

$$\mathbf{A}\begin{bmatrix}\mathbf{v}\\ \mathbf{T}\end{bmatrix} = -l\begin{bmatrix}\dfrac{1}{\rho}(\mathbf{n}\cdot\mathbf{T})\\ \lambda(\mathbf{n}\cdot\mathbf{v})\mathbf{I} + \mu(\mathbf{n}\otimes\mathbf{v} + \mathbf{v}\otimes\mathbf{n})\end{bmatrix},$$

$$\boldsymbol{\Lambda} = l\operatorname{diag}\{c_1, -c_1, c_2, -c_2, c_2, -c_2, 0, 0, 0\},$$

$$\boldsymbol{\Omega}\begin{bmatrix}\mathbf{v}\\ \mathbf{T}\end{bmatrix} = \begin{bmatrix}
\mathbf{n}\cdot\mathbf{v} - \dfrac{1}{c_1\rho}\mathbf{N}_{00} : \mathbf{T}\\
\mathbf{n}\cdot\mathbf{v} + \dfrac{1}{c_1\rho}\mathbf{N}_{00} : \mathbf{T}\\
\mathbf{n}_1\cdot\mathbf{v} - \dfrac{1}{c_2\rho}\mathbf{N}_{01} : \mathbf{T}\\
\mathbf{n}_1\cdot\mathbf{v} + \dfrac{1}{c_2\rho}\mathbf{N}_{01} : \mathbf{T}\\
\mathbf{n}_2\cdot\mathbf{v} - \dfrac{1}{c_2\rho}\mathbf{N}_{02} : \mathbf{T}\\
\mathbf{n}_2\cdot\mathbf{v} + \dfrac{1}{c_2\rho}\mathbf{N}_{02} : \mathbf{T}\\
\mathbf{N}_{12} : \mathbf{T}\\
(\mathbf{N}_{11} - \mathbf{N}_{22}) : \mathbf{T}\\
\left(\mathbf{N}_{11} + \mathbf{N}_{22} - \dfrac{2\lambda}{\lambda + 2\mu}\mathbf{N}_{00}\right) : \mathbf{T}
\end{bmatrix}, \quad \boldsymbol{\Omega}^{-1\mathrm{T}} = \frac{1}{2}\begin{bmatrix}
\mathbf{n} & -\rho[(c_1 - c_3)\mathbf{N}_{00} + c_3\mathbf{I}]\\
\mathbf{n} & \rho[(c_1 - c_3)\mathbf{N}_{00} + c_3\mathbf{I}]\\
\mathbf{n}_1 & -2c_2\rho\mathbf{N}_{01}\\
\mathbf{n}_1 & 2c_2\rho\mathbf{N}_{01}\\
\mathbf{n}_2 & -2c_2\rho\mathbf{N}_{02}\\
\mathbf{n}_2 & 2c_2\rho\mathbf{N}_{02}\\
0 & 4\mathbf{N}_{12}\\
0 & \mathbf{N}_{11} - \mathbf{N}_{22}\\
0 & \mathbf{I} - \mathbf{N}_{00}
\end{bmatrix}.$$

2.2. Grid-Characteristic Method

After making the change of variables $\boldsymbol{\omega} = \boldsymbol{\Omega}\mathbf{u}$, the governing system of equations splits into N independent scalar transport equations (N is the order of the system):

$$\dot{\boldsymbol{\omega}} + \boldsymbol{\Lambda}\frac{\partial\boldsymbol{\omega}}{\partial\xi} = 0.$$

The one-dimensional transport equations are solved with the help of characteristics. At the time level $n+1$, a characteristics is issued from the node m at which we want to obtain the solution. Then the corresponding component of the vector $\mathbf{v}$ is transferred from the intersection point of the characteristic with the nth level to the point ξ_m^{n+1}:

$$\omega_i^{n+1}(\xi_m) = \omega_i^n(\xi_m - \lambda_i\tau).$$

If the characteristic misses a node, then some method (usually interpolation) is used to reconstruct the solution at the given point. The reconstruction method chosen at the preceding layer determines the degree of approximation of the grid-characteristic difference scheme. First- and second-order accurate grid-characteristic schemes were obtained in [2]. A hybrid grid-characteristic scheme was used to solve problems in solid dynamics on rectangular grids in [5] and on triangular grids in [6, 7]. In [8] higher order accurate grid-characteristic methods were obtained, which satisfy the monotonicity criteria also presented in [8]. In this paper, we follow the method described in [6, 7].

After all the components of $\mathbf{v}$ were transferred, the solution is recovered as

$$\mathbf{u}^{n+1} = \mathbf{\Omega}^{-1}\boldsymbol{\omega}^{n+1}.$$

2.3. Boundary Conditions

At the material interfaces, we considered contact of the medium with empty pores (free boundary) or with liquid-filled pores (free slip). The boundary conditions at the interface between the medium and an inclusion were set in explicit form, which makes it possible (a) to weaken the constraints imposed on the positions and orientations of the inhomogeneities; (b) to take into account inhomogeneities with a nearly zero volume, but a finite surface area; and (c) to improve the numerical accuracy of computed microscopic inhomogeneities with sizes comparable to one grid cell. An unstructured triangular mesh allows one to describe any shape of inhomogeneities (cavities) inside the rock: pores or plane cracks.

On the outer boundary of the integration domain, we set the total absorption conditions. On the top boundary of the integration domain and on the crack boundaries, we specified the free surface condition

$$\mathbf{T}\cdot\mathbf{p} = 0,$$

where $\mathbf{p} = \mp\mathbf{n}$ defines a (unit) normal to the surface of the domain (or of a crack in the case of the boundary condition specified on a crack boundary). The minus and plus signs correspond to the left and the right boundaries of the domain (crack), respectively.

2.4. Interpolation in a Triangle

The velocity and stress fields were recovered by not linear interpolation in each triangle, but with the use nodal values as continuous piecewise quadratic functions. This made the numerical method monotone and allowed us to avoid spurious oscillations of the solution. The simulation technique proposed is original and was used by the authors in [9–16]. It produces high-order accurate wave fields in arbitrary randomly inhomogeneous media.

3. NUMERICAL RESULTS

The computational domain was 80 × 160 mm in size. It included a rectangular subdomain of 60 × 100 mm in size with nonconnected circular pores. The diameter of each pore was 1 mm, and the minimum distance between them was 0.5 mm. The minimum length of an internal grid edge was equal to 0.03 mm. The density of the grid was identical in the entire integration domain. Overall, the integration domain contained on the order of 11 million vertices (grid nodes).

On the top and bottom boundaries of the integration domain, we set the absorption conditions to prevent reflection from these boundaries and to imitate a continuous medium around the computational domain. The pores inside the rectangular domain were randomly distributed. Their coordinates were calculated using a random-number generator. Identical pore distributions were ensured for the same porosity at different fillers. The porosity was specified as follows: 5% (370 pores), 10% (737 pores), 15% (1104 pores), 20% (1467 pores), and 22% (1693 pores). The parameters of the ambient medium and the pore fillers are given in the table.

A liquid filler in the pores was specified by the free slip condition on the pore boundaries, which preserves only the orthogonal force on the boundary. The pore boundaries with no filler were computed in a

No.	Substance	Density ρ, kg/m^3	Speed of P-waves V_p, m/s	Speed of S-waves V_s, m/s
1	Ambient medium	2623	3371	2620
2	Solid filler	910	2909	1875
3	Liquid filler	1030	1475	50*

* Purely technical value required for the computational process.

similar manner to a free surface. The boundary of each pore was distinguished and calculated explicitly without using averaging methods.

The excitation was specified by a single plane compressional wave. Its front was 0.02 м away from the surface of the porous medium. Let us describe the types of waves generated in the interaction of an elastic wave with a porous medium and the features of wave propagation depending on the level of porosity and the physical characteristics of the filler. Consider the interaction of a plane wave with a single pore, which can be empty, water-filled, or solid-filled. Figure 1 shows wave patterns at six times: before, at the time, and after the front passes the pore for three filler types.

An analysis was performed for the case of no filler (Fig. 1a) and for two filler types: water (Fig. 1b) and solid (Fig. 1c). The empty pores, which, as was noted in Section 2, were described by the free-boundary model, do not transmit the elastic wave into the pore. The compressional wave reflects from its surface to form a primary (compressional) reflected wave (PP) and a secondary (shear) reflected wave forming an exchange one (PS). After the front passes the pore, it leaves behind a discontinuity, which is gradually reduced due to diffraction (Fig. 1a). In the case of a water-filled pore, part of the wave pulse is transmitted into the pore, while the other part reflects. The reflection gives rise to a primary reflected wave (PP) propagating in the opposite direction (upward) and a secondary wave, generating an exchange reflected one (PS). The elastic energy that was transmitted into the pore is partially transmitted through it, while the rest of the wave again reflects from the pore boundaries (Fig. 1b). Solid-filled pores reflect less energy toward the daytime surface than those with other fillers. This is caused by the fact that lower of the physical parameters of the solid filler are less contrasting against the ambient medium. Accordingly, the front of a transmitted primary wave decays minimally when propagating through such a pore.

The initial stage of the incident wave front travelling in an elastic continuous medium is presented in Fig. 2a. When the front reaches the surface of the porous medium, part of the wave is reflected. First, the waves reflected from the individual pores propagate separately (Fig. 2b), but they soon interfere to form a single wave packet travelling upward toward the daytime surface (Fig. 2c).

Later, the pattern becomes more complex. The wave penetrates deep into the porous medium and reflects from the next of "layers" of pores (Fig. 2d). However, travelling in the opposite direction, these waves again reflect from the upper layers, so multiple waves emerge. Accordingly, the study of the reflection coefficient is reduced to analyzing the behavior of the reflected waves. In the case of water-filled pores, in addition to the multiple waves, there appear waves transmitting into the pores and then leaving them. They also interfere with the reflected waves. As a result, the wave pattern becomes even more complex. Obviously, the wave pattern depends strongly on the degree of porosity, which can be seen in Fig. 3. Primarily, the intensity of the reflected waves increases with porosity. Moreover, the front of the transmitted wave decays and deforms more quickly.

The filler type also plays an important role in the character of the wave propagation. The difference between empty and water-filled pores is highly pronounced (primarily, due to the presence or absence of a continuous medium inside the pores), whereas the difference between liquid and solid fillers is much less so, although being noticeable (Fig. 4).

It should be noted that the absence of pores in Figs. 4b and 4c is explained by the fact that a grid is not drawn on them (which hinders the visual analysis due to its fineness). Since the nodal values inside empty pores are zero, their content is treated by the program as a background, which allows them to be visualized (Fig. 4a). The pores with a liquid or solid filler receive much more energy, and this transmitted wave decays more slowly. This can be seen in Fig. 1, as well as in Fig. 4a, where we can see an upper layer of empty pores, while, for the other media, only the pores nearest to the incident wave can be observed. Moreover, in water-filled and empty pores, shear waves do not propagate, while propagation of these waves in a solid filler is significant.

For a quantitative analysis of the problem, including the computation of targeted decay and reflection coefficients, we have to analyze the one-dimensional graphs of the solution. However, as can be seen in

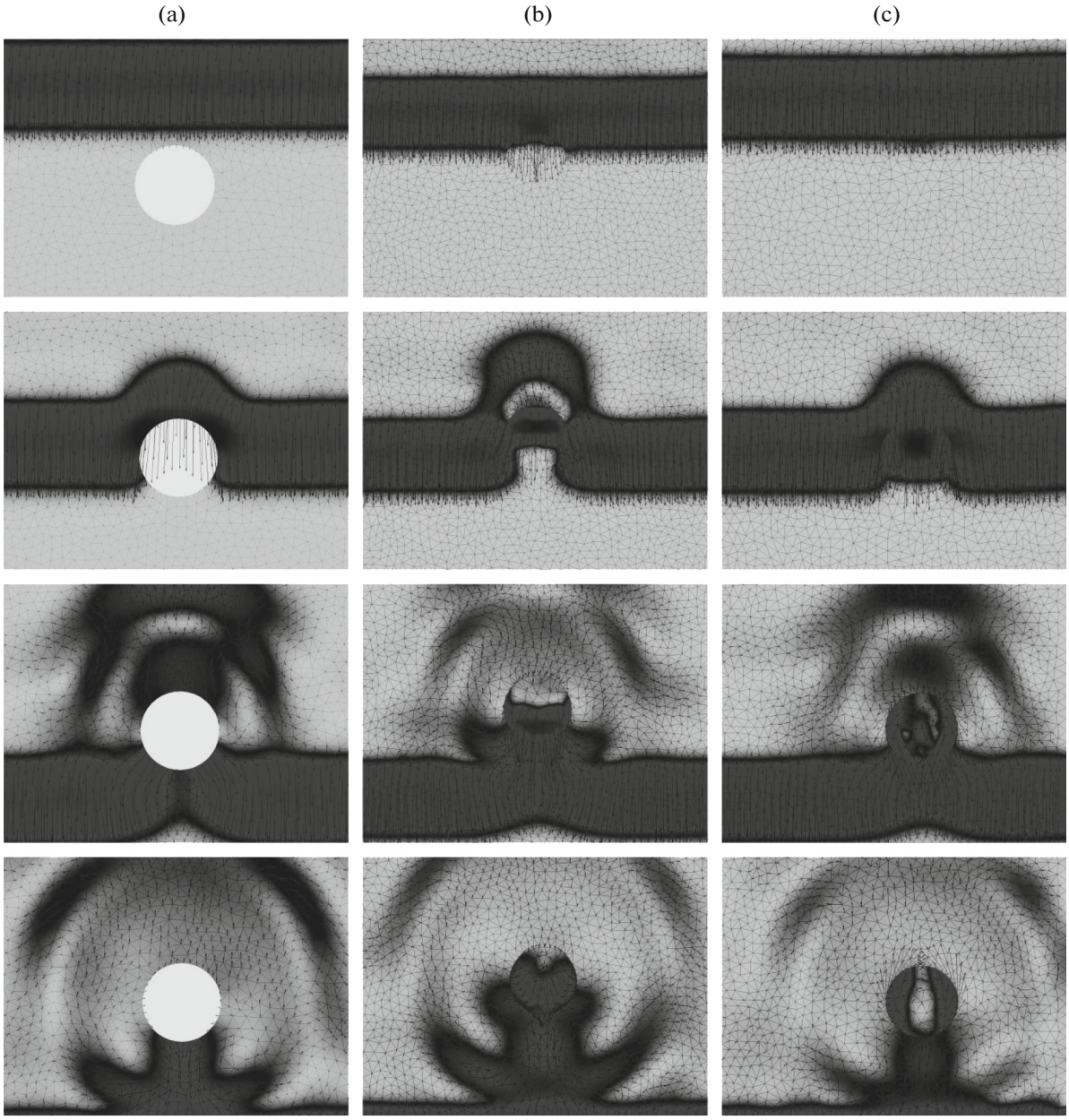

Fig. 1. Wave patterns of the front propagating through a single pore for different fillers: (a) empty pores, (b) water, and (c) solid.

Figs. 2–4, the solution of the problem is asymmetric. This is associated primarily with the nonuniformity of the pore distribution inside the rock. To overcome this difficulty, an averaging procedure has to be applied to the results. For this purpose, we constructed vertical cross sections beginning near the top boundaries and ending on the bottom boundary of the integration domain. They were processed and averaged, and one-dimensional plots of wave propagation were drawn at regular intervals. In the given model, we used 11 cross sections with 350 points in each. The distance between the points was 0.04 mm. Thus, at most two points could lie within a singly pore. Two cross sections were separated by a distance of 0.5 mm. The horizontal coordinates were chosen with allowance for effects on the boundaries of the porous medium that are not characteristic for central parts and associated with a sharp drop in the wave amplitude on the boundary. Thus, the cross section nearest to the boundary was 0.5 mm away from it. With the help the resulting one-dimensional plots, we can easily observe the propagation of the incident wave, the separation of reflected waves from it, and its decay (see Fig. 5, which was plotted for empty pores with 15% porosity). These data are analyzed below.

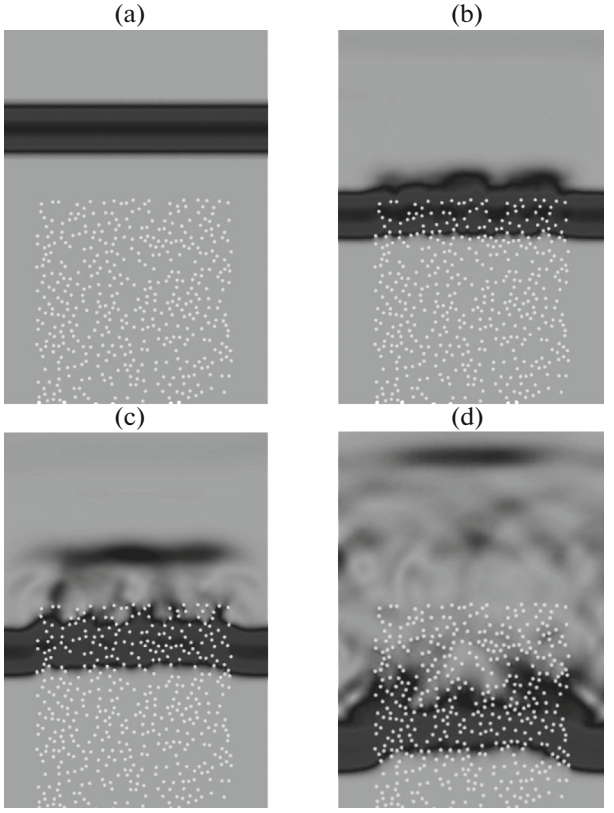

Fig. 2. Propagation of a plane wave through a medium with empty pores.

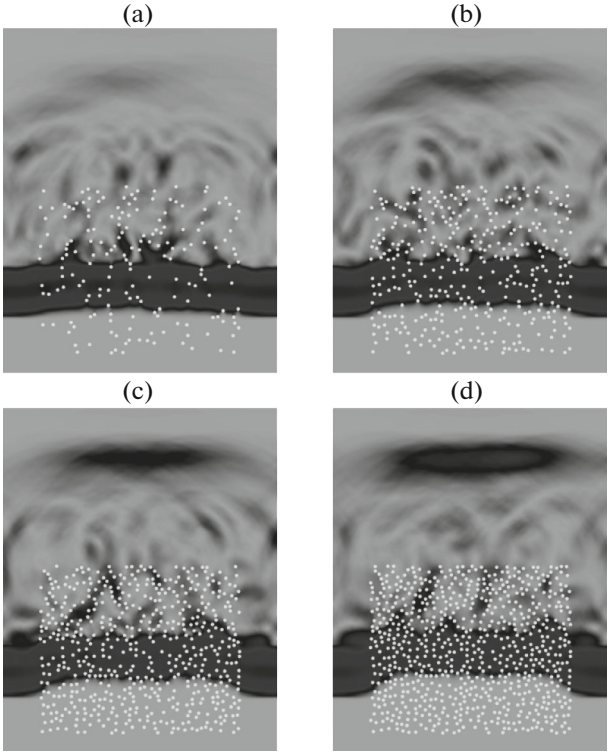

Fig. 3. Wave pattern at the same time for porosity ranging from 5 to 20%.

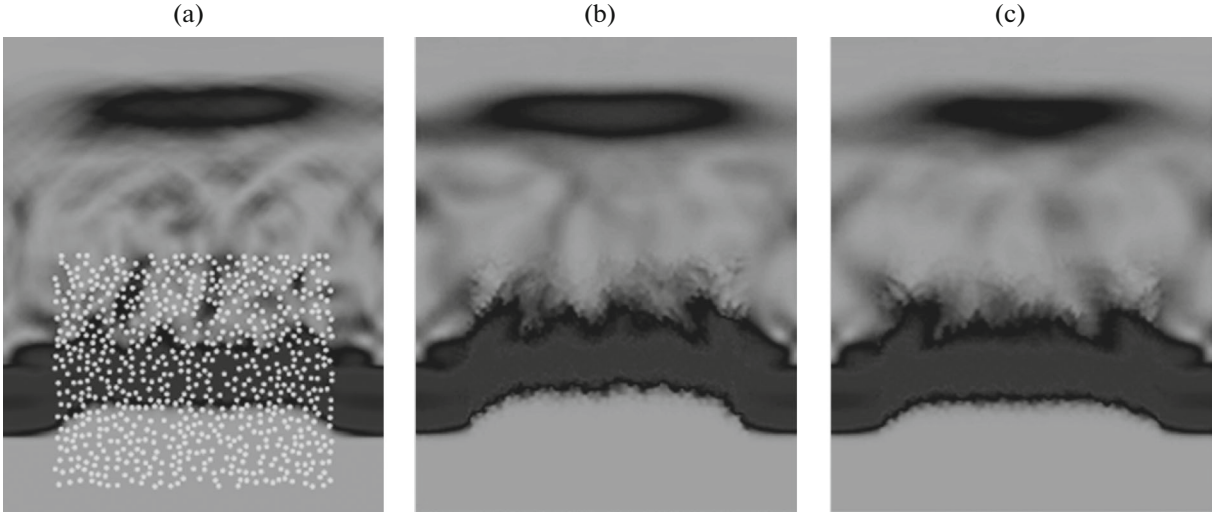

Fig. 4. Wave pattern at the same time for media with different filler types at 20% porosity: (a) empty pores, (b) water, and (c) solid.

According to the conventional definition, the decay factor (K_{dec}) is the inverse of the time over which the wave amplitude decays by $e = 2.718$ times. The decay factor was computed as follows.

1. The time was chosen at which the wave amplitude became e times smaller. Since time in the numerical computation was discrete, we chose the moment when the wave amplitude was the nearest to $V = V_0/e$, but no less than this value.

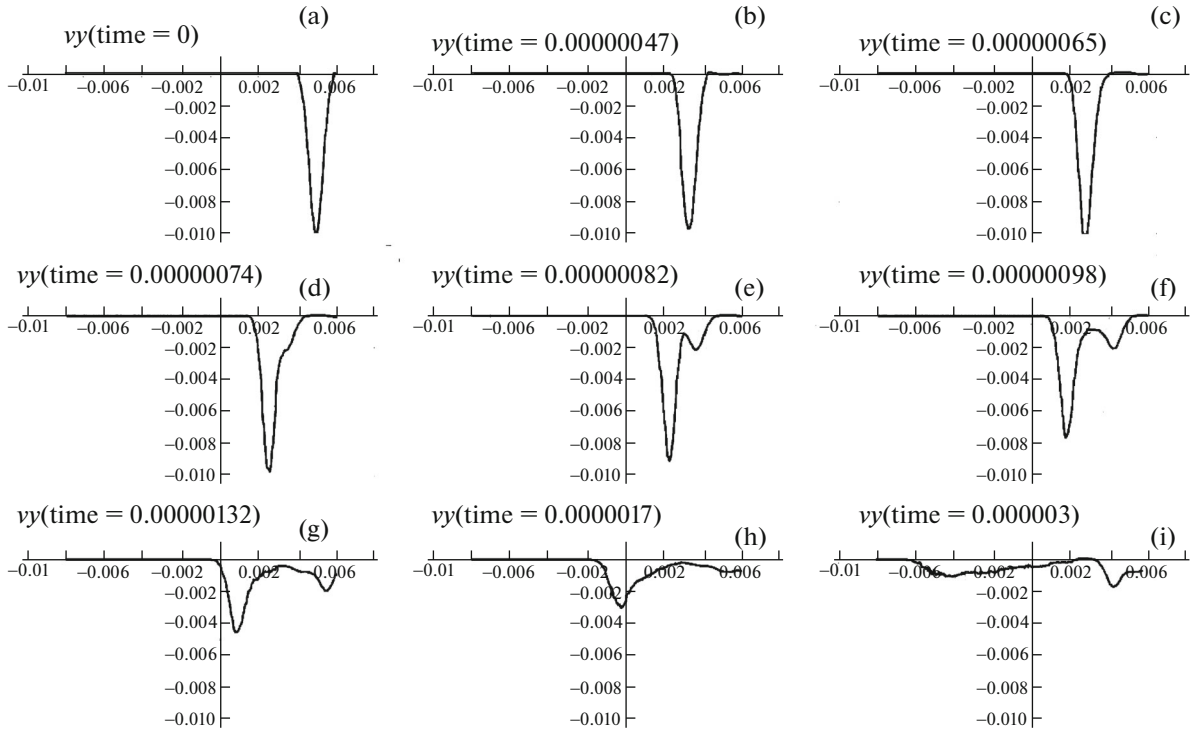

Fig. 5. (a), (b) Propagation of an incident wave in the direction of a porous medium; (c), (d) the formation of the first reflected wave; (e), (f) separation of the first reflected wave; (g), (h) continued separation of the reflected waves and gradual decay of the incident wave; and (i) the incident wave has nearly reached the lower edge of the porous medium and has nearly disappeared. Wave processes inside the medium continue.

2. The moment was calculated when the wave entered the porous medium. Since the results were also recorded at a finite number of points, we chose the point nearest in coordinate to the surface of the explored domain (in fact, already lying inside the medium) and the moment was chosen when the velocity at this point became nonzero for the first time.

3. The latter quantity was subtracted from the former.

4. The inverse of the quantity obtained in item 3 was computed. This was the decay factor of the wave in the given medium. The initial amplitude of the incident wave was equal to 0.01 m/s. To compute the decay factor, according to item 2, we chose the first moment when the wave amplitude became ≤ 0.0037 m/s.

The computations were performed for media with porosity ranging from 5 to 22%. As was expected, the wave decayed faster with growing porosity (Fig. 6).

For different filler types, the decay factor as a function of porosity behaves differently. For each filler, the decay factor was plotted against porosity in percent (Fig. 7).

All the dependences are nearly linear. For low porosity, the plots for different fillers nearly coincide, which means that they are indistinguishable under these conditions. As the porosity grows, the difference becomes more noticeable. In the considered range of porosity, the proportionality constant for the decay factor is approximately equal to 0.6 ± 0.1.

Next, the reflection coefficient from the surface of the porous medium was analyzed as a function of the degree of porosity and the filler type. According to the conventional definition, the reflection coefficient is the ratio of the amplitude of the first reflected wave to the amplitude of the incident wave. The computations were performed as follows.

1. The incident wave amplitude was specified as the average amplitude up to the time when the wave reaches the porous medium. This time was calculated according to item 2 in the above description of computing the decay factor.

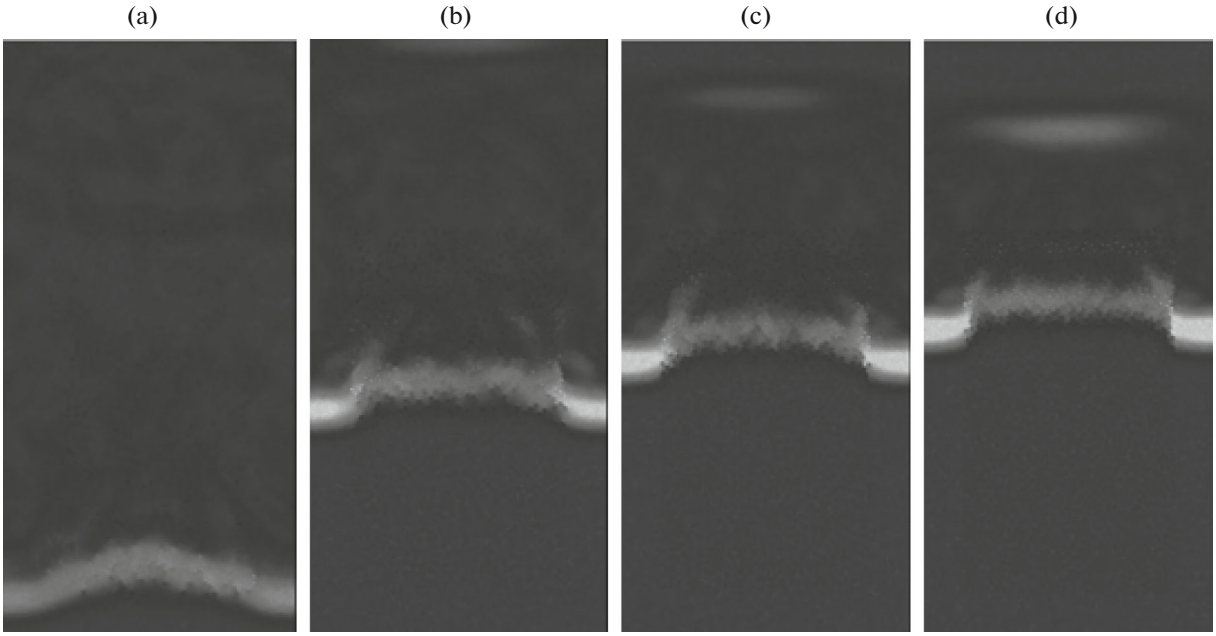

Fig. 6. The wave pattern at the times when the incident wave amplitude reaches 0.0037 m/s for media with porosity of (a) 5%, (b) 10%, (c) 15%, and (d) 20%.

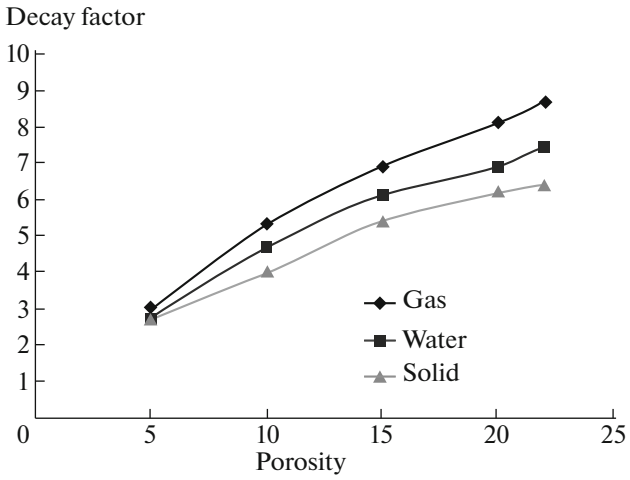

Fig. 7. Decay factor vs. porosity in % for various fillers.

2. By inspecting one-dimensional plots of the wave velocity, a moment was chosen when the first reflected wave had formed and begun to move in the opposite direction to the incident wave. The average amplitude of this wave in its travel toward the top boundary of the integration domain was computed.

3. The reflection coefficient was calculated as the ratio of the first amplitude to the second one.

In contrast to the analysis of the decay factor as a function of porosity (Fig. 6), the two-dimensional wave pattern is not very informative for a visual analysis of the same dependence for the reflection coefficient. Accordingly, for illustrative purposes, we present one-dimensional plots fixing the amplitude of the first reflected wave at the same time for different porosities (Fig. 8).

The type of the filler also plays an important role in the wave reflection from the porous medium. The reflection coefficient as a function of porosity for various types of fillers is shown in Fig. 9.

All the dependences are also nearly linear. The proportionality constant is approximately equal to 0.8 ± 0.05, which is noticeably higher than that for the decay factor. Moreover, we can conclude that, for

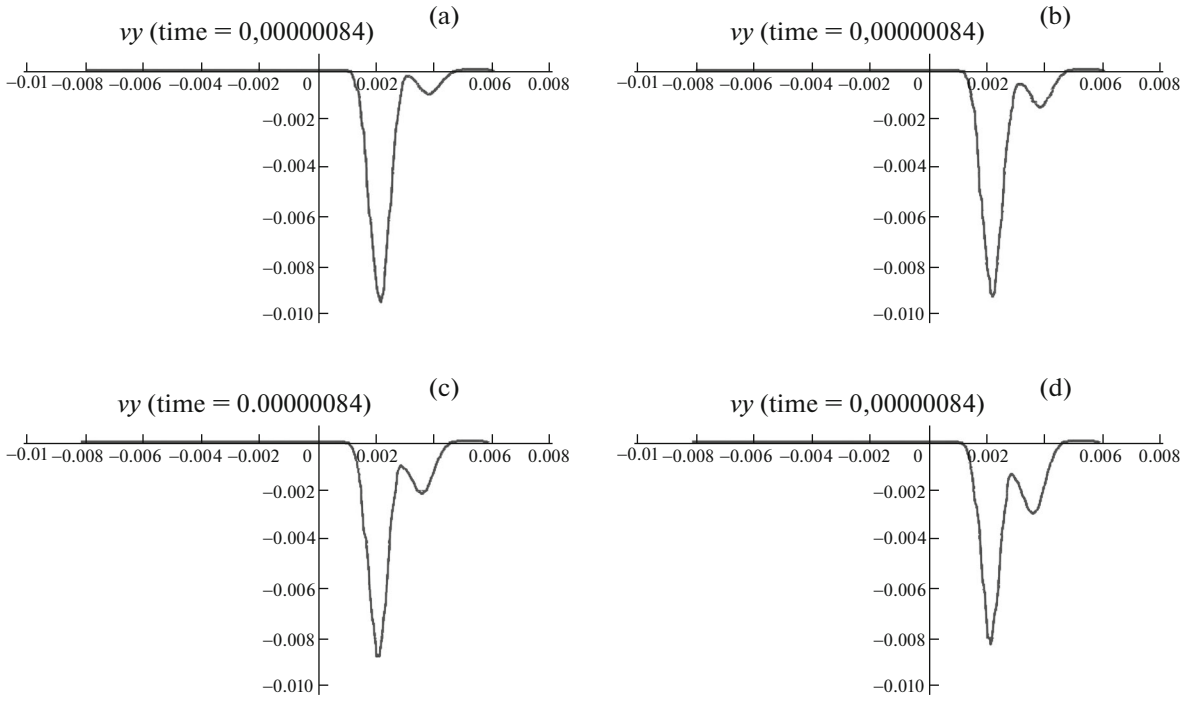

Fig. 8. Amplitude of the first reflected wave for media with various porosities (empty pores).

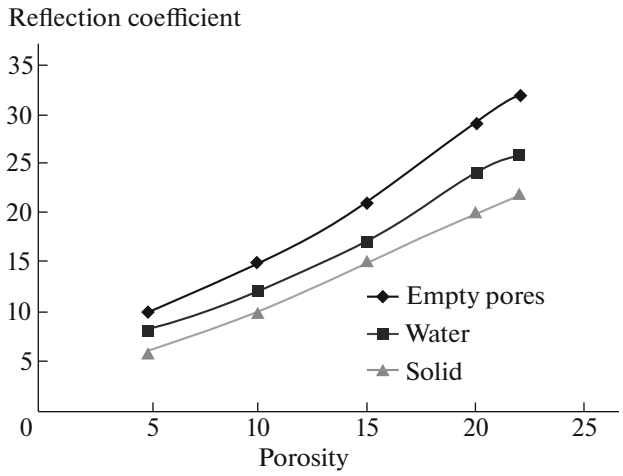

Fig. 9. Reflection coefficient vs. porosity in % for various fillers.

any porosity (including low ones), the reflection coefficient depends on the type of the filler. For example, in the case of empty pores, it is roughly 20% higher than in the case of liquid-filled pores.

CONCLUSIONS

1. Fundamentally different mechanisms of elastic wave propagation through empty and water-filled pores were detected. Specifically, an elastic wave is not transmitted into a pore in the former case and is multiply reflected inside it in the latter case.

2. It was found that the reflection coefficient is nearly a linear function of porosity with a proportionality constant of 0.8. This finding suggests that the use of reflection amplitudes is promising for the prediction of porosity.

3. It was found that the decay factor is also a nearly linear function of porosity, but with a proportionality constant of 0.6.

4. The sensitivity of the reflection and decay coefficients as functions of porosity increases from solid to liquid fillers and from liquid-filled to empty pores by roughly 20%.

5. As a further study, it seems reasonable to investigate the reflection and scattering of elastic waves in a porous medium in a three-dimensional formulation, which can change some of the quantitative results obtained in this paper.

REFERENCES

1. B. Gurevich, "Effect of fluid viscosity on elastic attenuation in porous rocks," Geophysics **67**, 264–270 (2002).
2. K. M. Magomedov and A. S. Kholodov, *Grid-Characteristic Numerical Methods* (Nauka, Moscow, 1988) [in Russian].
3. I. B. Petrov and A. S. Kholodov, "Regularization of discontinuous numerical solutions of equations of hyperbolic type," USSR Comput. Math. Math. Phys. **24** (4), 128–138 (1984).
4. I. B. Petrov and A. S. Kholodov, "Numerical study of some dynamic problems of the mechanics of a deformable rigid body by the mesh-characteristic method," USSR Comput. Math. Math. Phys. **24** (3), 61–73 (1984).
5. A. S. Kholodov and Ya. A. Kholodov, "Monotonicity criteria for difference schemes designed for hyperbolic equations," Comput. Math. Math. Phys. **46** (9), 1560–1588 (2006).
6. E. Kvasov, I. B. Petrov, and F. B. Chelnokov, "Computation of wave processes in heterogeneous space structures," Mat. Model. **21** (5), 3–9 (2009).
7. I. E. Kvasov, S. A. Pankratov, and I. B. Petrov, "Numerical simulation of seismic responses in multilayer geologic media by the grid-characteristic method," Math. Model. Comput. Simul. **3** (2), 196–204 (2011).
8. I. B. Petrov and F. B. Chelnokov, "Numerical analysis of wave processes and fracture in layered targets," Comput. Math. Math. Phys. **43** (10), 1503–1519 (2003).
9. I. E. Kvasov and I. B. Petrov, "High-performance computer simulation of wave processes in geological media in seismic exploration," Comput. Math. Math. Phys. **52** (2), 302–313 (2012).
10. V. B. Leviant, I. B. Petrov, and V. B. Chelnokov, "Cluster nature of the scattered seismic effect produced by a zone of diffuse cavities and fractures in massive rock," Geofizika, No. **6**, 5–19 (2005).
11. V. B. Leviant, I. B. Petrov, and I. E. Kvasov, "Numerical simulation of wave response of subvertical macrofractures, possible fluid-conducting channels," Tekhnol. Seismorazvedki, No. **4**, 4–16 (2011).
12. I. E. Kvasov, V. B. Leviant, and I. B. Petrov, "Numerical simulation of direct responses to sheet zones with subvertical fluid-saturated mesofractures," Tekhnol. Seismorazvedki, No. **4**, 19–35 (2013).
13. I. E. Kvasov and I. B. Petrov, "Numerical study of the anisotropy of wave responses from a fractured reservoir using the grid-characteristic method," Math. Model. Comput. Simul. **4** (3), 336–343 (2012).
14. I. E. Kvasov, V. B. Leviant, and I. B. Petrov, "Numerical modeling of direct responses from productive reservoirs with vertical fluid-saturated meso-fractures," *76th EAGE Conference and Exhibition 2014, June 16–19, 2014, Amsterdam RAI*. doi 10.3997/2214-4609.20141192
15. I. E. Kvasov, V. B. Leviant, I. B. Petrov, M. V. Muratov, "Numerical modeling of responses from fluid-filled macrofractures with boundary conditions specified on fracture surfaces," *76th EAGE Conference and Exhibition 2014, June 16–19, 2014, Amsterdam RAI*. doi 10.3997/2214-4609.20141524
16. I. E. Kvasov, I. B. Petrov, A. V. Sannikov, and A. V. Favorskaya, "Computer simulation of three-dimensional dynamic processes by applying the grid-characteristic method on unstructured tetrahedral meshes," Zh. Inf. Tekhnol., No. 9, 28–30 (2011).

Translated by I. Ruzanova